Dalton Transactions

ROYAL SOCIETY OF CHEMISTRY

PAPER

View Article Online
View Journal | View Issue

Cite this: *Dalton Trans.*, 2025, **54**, 13085

Synergistic WO_3-PBI hybrid electrochromic materials with an enhanced diffusion coefficient and cycling reversibility inspired by the "Big Rocks" theory

Chunxia Hua, Huanyu Tan, Shujin Ma, Jiaxue Hou, Ming Gong, Jia Chu, Xiaoqin Wang and Shanxin Xiong *

The key technology underlying intelligent energy conversion and display systems hinges on high-performance electrochromic materials. To drive their electrochemical redox reactions, facilitating ion/electron transport and intercalation/deintercalation *via* the rational design of a highly connected electrode structure is critical. However, persistent challenges include inadequate interconnection between active species – stemming from the inherent limitations of simple inorganic materials and severe performance degradation during long-term electrochemical cycling. To address the interconnection issue of active species, we propose a novel inorganic/organic hybrid film inspired by the "Big Rocks" theory: PBI derivatives are dip-coated onto a pure WO_3 film to form a secondary structure. The effects of optimal preparation parameters on the experimental outcomes were analyzed. The WO_3/PBI hybrid film exhibited a reversibility of approximately 98% after 1400 cycles, whereas the WO_3 film retained only 47% reversibility after 500 cycles. The coloration efficiency of the WO_3/PBI hybrid film (245 cm^2 per C) was more than twice that of the WO_3 film (114 cm^2 per C). The superior cycling durability and coloration efficiency of the hybrid film are attributed to three key factors: (1) surface modification by the organic component, (2) an enhanced ion diffusion coefficient, and (3) improved electrochemical activity enabled by the incorporation of PBI-CB derivatives. Additionally, the remarkable electrochromic performance of the WO_3/PBI material was demonstrated, showcasing its potential as an intelligent strategy for automatic optical switching using hybrid materials. These findings will pave the way for next-generation intelligent technologies geared toward building a sustainable and livable future.

Received 17th June 2025,
Accepted 4th August 2025

DOI: 10.1039/d5dt01423a

rsc.li/dalton

Introduction

One of the paramount objectives of contemporary technology is to enhance energy efficiency and promote energy conservation, primarily through the leveraging of new technologies and "smart" materials.[1–4] "Smart" materials exhibit multiple functional states that can be altered by external stimuli and evolve dynamically over time. Electrochromic materials (ECs), which reversibly change color in response to an electric field, form the basis of low-power-consumption electrochromic devices (ECDs), such as smart windows, rearview mirrors, electronic papers, helmet visors, climate-adaptive building shells and sensors.[5,6] Over the past decade, interest in organic/inorganic hybrid electrochromic materials has surged owing to their capacity to improve the electrochemical and electrochromic properties of devices.[7,8]

EC materials are primarily grouped into inorganic and organic categories. Compared to organic EC materials, inorganic materials typically exhibit superior chemical stability and cycling durability, making them well-suited for "Smart Windows" and large-scale data display applications. Tungsten trioxide (WO_3) remains the most promising inorganic EC material due to its relatively high coloring efficiency, broad dynamic optical modulation range, excellent environmental stability and ability to intercalate lithium ions (Li^+), a critical attribute that underpins its suitability for EC applications.[9] After years of intensive research and development, WO_3-based EC "Smart Windows" have finally evolved into commercially viable products. Broad optical modulation capability and robust electrochemical stability are generally recognized as essential prerequisites for the practical deployment of EC materials. However, performance degradation, often attributed to the ion-trapping effect, after hundreds or thousands of

College of Chemistry and Chemical Engineering, Xi'an University of Science and Technology, Xi'an 710054, China. E-mail: xiongsx@xust.edu.cn

electrochemical cycles, has severely impeded their widespread commercialization.[10] Although the constant-current-driven ion extraction method has been proposed to restore electrochromic performance, it fails to fundamentally eliminate such degradation when irreversible structural changes and defect formation occur during cycling.

Despite the high coloring efficiency and the capacity to intercalate lithium ions of WO_3-based materials, they still lack a large dynamic modulation range and good cycling stability for practical applications. To further enhance the EC performance of WO_3, several studies have been published that introduce various nanostructured forms of WO_3, including nanowires, nanorods, nanosheets, inverse opal porous WO_3 films and hybrid organic–inorganic EC systems.[11–15] Additionally, composite materials such as WO_3/NiO, P_5W_{30}/WO_3, and WO_3/PANI have also been explored to improve EC performance.[16–18] Among these strategies, preparing a WO_3 hybrid film represents an effective and straightforward approach for enhancing its EC performance. It is well established that PBI derivatives constitute an important class of EC materials, owing to their exceptional photochemical and thermal stability, as well as efficient visible-light absorption. Notably, the geometrical PBI dimer (PBI-CB) exhibits strong fluorescence and high photochemical stability in the solid state. Furthermore, our previous research has demonstrated that PBI-CB is a promising small organic molecule for EC applications.[19] The structure of the selected PBI derivative, PBI-CB, is shown in Fig. S1. Therefore, in this study, we aim to further enhance the EC performance of WO_3 films by integrating the porous structure of the WO_3 film with the non-planar conformation of PBI derivatives. It is anticipated that the incorporation of nanopores will increase the surface area, thereby providing a larger interface between WO_3 and the electrolyte, which can significantly enhance the diffusion coefficient of Li^+ ions. Furthermore, the integration of PBI within the porous WO_3 film is expected to effectively mitigate slow EC switching, which can result from obstructed electron and ion flow due to potential holes or cracks in the porous structure.

The objective of this work is to expand the methodologies for enhancing the electrochromic properties of WO_3 materials by utilizing organic/inorganic composite materials. Through orthogonal design experiments, we systematically investigated the optimal preparation conditions of the hybrid film and analyzed the impact of various preparation factors on the experimental outcomes. Photo-electrochemical and characterization studies revealed that, compared to pure WO_3 films, the WO_3/PBI hybrid film exhibits an optimized interface and continuous structure, resulting in superior performance as a high-performance electrochromic electrode. This includes significant optical modulation, excellent coloring efficiency, and robust cycling stability. Moreover, the exploration of the WO_3/PBI film *via* a simple, cost-effective, and scalable method may broaden the range of materials suitable for the preparation of organic/inorganic hybrid electrochromic materials, thereby facilitating their widespread industrial applications such as smart windows, displays, and other optical devices.

Results and discussion

Orthogonal design and test

In this paper, our research objectives focus on investigating the impact of interfacial modification with a PBI derivative on the electrochemical and electrochromic properties of WO_3 films. It is essential to examine the synergistic effects between the two components of the hybrid films and the post-processing of the films. During experiments assessing the influence of hybrid film components on EC performance, it is crucial to comprehensively consider various factors, including different deposition times of WO_3 and varying volumes of PBI derivatives. These tests are typically repeated multiple times to ensure reliable conclusions, which can lead to significant consumption of test materials and time. Therefore, the orthogonal experimental design method is generally employed to efficiently study the effects of multiple factors.[20]

As we know, the transmittance of WO_3 films is significantly influenced by the electrodeposition time. The transmittance of the WO_3 films is optimized for WO_3/PBI hybrid EC films prior to the study of their electrochemical performance. The electrochemical deposition curves and the corresponding transmittance spectra of the films with different deposition times are presented in Fig. S2 and S3. It is evident from these results that the transmittance of pure WO_3 films experiences a pronounced decline when subjected to extended electrodeposition times (>90 s). Consequently, it is imperative to employ a short electrodeposition time (<90 s) for the synthesis of hybrid WO_3/PBI films. The study of transmittance modulation of the EC-active film under varying electrodeposition times (for the WO_3 film) and diverse PBI contents under actual working conditions is of significant practical relevance. In addition, as established in our earlier report, the annealing process of the active film is crucial for the electrochemical performance of the films. Based on preliminary tests and analysis, we selected the orthogonal table L9 (33) for this three-factor and three-level experiment (Table S1), without considering the interactions between factors. The deposition time of the WO_3 film was set at three levels (30 s, 60 s and 90 s), the volume of PBI derivatives was set to three levels (30 μL, 60 μL and 90 μL at a concentration of 1×10^{-3} mol L^{-1}), and the post-processing temperatures were set to three levels (initial state, 100 °C and 130 °C). In the orthogonal test design, the three factors – deposition time of the WO_3 film (A), volume of PBI solution (B), and hot-press temperature (C) – were randomly arranged in the corresponding columns of the orthogonal table. This resulted in the orthogonal table shown in Table 1. For instance, test plan A1B1C1 in test No. 1 denotes a combination of 30 s deposition time (WO_3 film), 30 μL volume (PBI derivative) and no low-temperature annealing process. The remaining eight test plans followed a similar pattern. Experiments were conducted according to the orthogonal test table described above.

The nine sets of tests in Table 2 were analyzed as follows. All films exhibited high transmittance (>80%, 720 nm), as shown in Fig. S4. CV tests for the orthogonal test samples, conducted within a potential range from 1.0 V to −1.3 V at a scan

Table 1 The orthogonal table plans

Test no.	A Deposition time (WO_3, s)	B Volume (PBI-CB, μL)	C Curing temperature (°C)
1	1 (30)	1 (30)	1 (initial)
2	1	2 (60)	2 (100)
3	1	3 (90)	3 (120)
4	2 (60)	1	2
5	2	2	3
6	2	3	1
7	3 (90)	1	3
8	3	2	1
9	3	3	2

Table 2 The range analysis of the transmittance variation of the samples

Test No.	A Deposition time (WO_3, s)	B Volume (PBI-CB, μL)	C Curing temperature (°C)	Evaluation index
1	1 (30)	1 (30)	1 (initial)	46.8
2	1	2 (60)	2 (100)	6.7
3	1	3 (90)	3 (120)	74.4
4	2 (60)	1	2	6.3
5	2	2	3	11.4
6	2	3	1	0.7
7	3 (90)	1	3	42.3
8	3	2	1	64.8
9	3	3	2	78.7
*T*1	42.6	31.8	37.4	
*T*2	6.1	27.6	42.7	
*T*3	61.9	51.3	30.6	
R	55.8	23.7	12.1	

Range size: $R_A = 55.8 > R_B = 23.7 > R_C = 12.1$.

rate of 50 mV s^{-1}, are presented in Fig. S5. The corresponding transmittance–time curves during the CV process are shown in Fig. S6. All nine films exhibited distinct charge-transfer behavior during CV redox cycles. Notably, sample S9 showed the highest peak current density and the largest enclosed area within the CV curve. These nine films also demonstrated varying degrees of transmittance modulation. Specifically, S9 achieved the highest transmittance change, approximately 78.7%. The main value *Ti* is the arithmetic mean value of the test result index, that is, transmittance modulation at 720 nm, obtained from the test plans corresponding to any level of factor *i* (*i* = 1, 2, 3). For example, the three test plans corresponding to level 1 (30 s) of deposition time (WO_3 film) in column A yielded an arithmetic mean of *k*1 = (46.8 + 6.7 + 74.4)/3 = 42.6. Similarly, all other mean values can be calculated.

The purpose of the orthogonal design is to identify the primary factors influencing the test results and determine the optimal combination of factor levels. In practical applications, both electrochemical activity and transmittance modulation should be maximized. Therefore, the levels corresponding to the highest electrochemical activity and transmittance variation were selected based on the maximum mean values Δ*Ti*. The trend chart between factor levels and the mean values is shown in Fig. S7. Evidently, the results demonstrate that for factor A, the performance order was *T*3 > *T*1 > *T*2; for factor B, the trend was consistent with factor A (*T*3 > *T*1 > *T*2); and for factor C, the order was reversed (*T*2 > *T*1 > *T*3). Thus, the optimal level combination for the factors is A3B3C2, corresponding to a WO_3 film deposition time of 90 s, a PBI derivative volume of 90 μL, and an annealing temperature of 100 °C. Under these conditions, the maximum transmittance variation was achieved within the test range.

The range *R* is defined as the difference between the maximum and minimum arithmetic mean *Ti* values for any given factors, *i.e.*, $R = \max\{T1, T2, T3\} - \min\{T1, T2, T3\}$. The range values indicate the degree of influence of each factor on transmittance variation. Larger ranges signify greater changes in transmittance variation due to variations in factor levels. Therefore, the factor with the largest range has the greatest impact on the transmittance variation and is considered the main factor. The range analysis results are summarized in Table 2. From the data in Table 2, obviously, the results meet the equation $R_A > R_B > R_C$, respectively. From the above, it can be concluded that, for transmittance modulation of the WO_3/PBI hybrid films under varying WO_3 film deposition times (A), PBI derivative volumes (B) and annealing temperatures (C), the three factors are ranked in the order of A > B > C.

Electrochemical performance

Considering the target of this study and the results of orthogonal design, we first compare the morphology and electrochemical properties of WO_3 and WO_3/PBI hybrid films (S9). The WO_3/PBI hybrid film exhibits greater roughness, fewer cracks and a more continuous surface with distinct microstructural aggregates compared to the pure WO_3 film, which exhibits a smooth but loose surface (Fig. 1a and b). To verify the

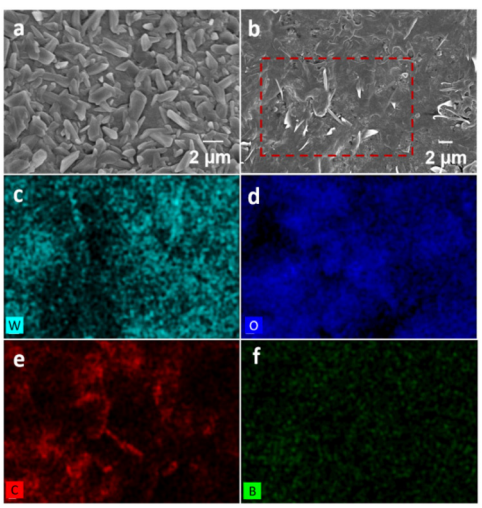

Fig. 1 SEM images of the pure WO_3 (a) and hybrid WO_3/PBI (b) films. EDS image of the specified area of the hybrid WO_3/PBI film ((c) W; (d) O; (e) C; (f) B).

composition and morphology of the microstructural aggregates on the surface of the WO_3/PBI hybrid film, scanning electron microscopy (SEM) coupled with EDS elemental mapping of a selected area was employed. Elements W, O, C and B were detected in a 180 nm × 180 nm region (Fig. 1c, d, e and f). As shown in Fig. 1, the WO_3/PBI film demonstrates uniform elemental distribution of W, C, and B. These results confirm that the WO_3 film is effectively covered by the PBI component, forming a more continuous hybrid film.[21,22] FTIR spectra of the WO_3 and WO_3/PBI films were also analyzed to further validate their differences (Fig. S8). In comparison with the absorption peaks of the ITO substrate, WO_3 film and WO_3/PBI hybrid film, two new peaks at 2923 cm^{-1} and 2852 cm^{-1} were detected in the WO_3/PBI hybrid film. These peaks are most likely attributed to the C–H stretching vibrations of the PBI component.[23] To further investigate the differences between these two films, XRD patterns of the WO_3 and WO_3/PBI hybrid films were recorded (Fig. S9). The XRD patterns of the ITO substrate and WO_3 film exhibit diffraction peaks assigned to ITO at 30.7° and 35.7° corresponding to the (022) and (012) planes, respectively. These characteristic diffraction peaks disappeared in the WO_3/PBI hybrid film, indicating complete coverage of the ITO substrate by WO_3/PBI,[24] consistent with the morphological changes observed in Fig. 1 and the organic component addition in Fig. S8.

To evaluate the role of the PBI derivative in the WO_3/PBI hybrid electrode design, the electrochemical and electrochromic (EC) characteristics of the WO_3/PBI hybrid film were compared with those of the pure WO_3 film under the same deposition time. Cyclic voltammetry (CV) curves illustrate the insertion (coloring) and de-insertion (bleaching) processes of the WO_3 film and WO_3/PBI hybrid film in a 1 mol L^{-1} PC/$LiClO_4$ electrolyte at a constant scan rate of 50 mV s^{-1} (Fig. 2). Upon Li^+ ion intercalation, the transparent WO_3 and WO_3/PBI films turn bluish or deep blue. Conversely, when Li^+ ions are deintercalated from the films, they gradually bleach and become transparent again. CV measurements reveal a relatively larger area under the CV curve and enhanced current density for the WO_3/PBI hybrid film, demonstrating that the introduction of the PBI derivative improves the ionic/electrical conductivity and strengthens the reaction kinetics of WO_3 in the electrolyte.[25] Repeated intercalation and deintercalation cycles of Li^+ ions result in reversible switching between coloration and bleaching of the films.

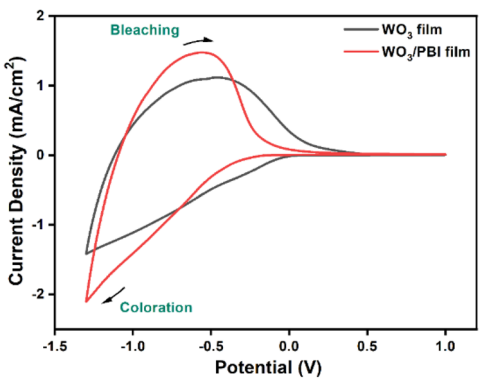

Fig. 2 Cyclic voltammetry (CV) curves of the WO_3 and WO_3/PBI hybrid films. Note: each CV curve was obtained at a scan rate of 50 mV s^{-1} in the 1 mol L^{-1} PC/$LiClO_4$ electrolyte.

To further understand the electrochemical kinetics, the diffusion coefficient of Li^+ was calculated. The diffusion coefficient (D) of the Li^+ ions in the WO_3 and WO_3/PBI hybrid films can be derived from the CV results using the Randles–Sevcik equation:[26,27]

$$D^{1/2} = j_p/2.69 \times 10^5 n^{3/2} C_0 v^{1/2} \quad (1\text{–}1)$$

where D is the diffusion coefficient ($cm^2\ s^{-1}$), j_p is the average insertion and de-insertion current density (mA cm^{-2}), n is the number of electrons, C_0 is the concentration (mol cm^{-3}) of Li^+ ions in the electrolyte, and v is the scan rate (mV s^{-1}). The diffusion coefficients obtained are 8.6 × 10–12 $cm^2\ s^{-1}$ and 14.9 × 10^{-12} $cm^2\ s^{-1}$ for the WO_3 and WO_3/PBI hybrid films, respectively. The diffusion coefficient of Li^+ ions in the WO_3 electrode significantly increases after interfacial modification with PBI derivatives. As shown in Fig. 1, there is also a notable reduction in defects and cracks in the film after interfacial modification with the PBI derivative, suggesting that the enhancement in the diffusion coefficient may be attributed to the increased continuity of the active substance. The higher packing density of the redox-active substance correlates with a higher diffusion coefficient of Li^+ ions for the WO_3/PBI hybrid film in the $LiClO_4$ electrolyte.

Electrochromic performance

Chronoamperometry (CA) is a classic technique for examining the reversibility of the coloring (intercalation) and bleaching (deintercalation) process of electroactive materials. Here, CA was performed to determine the reversibility of the coloration and bleaching process using a three-electrode system. The working electrodes consisted of WO_3 and WO_3/PBI films, while the counter and reference electrodes were Pt wires and an Ag/AgCl electrode, respectively. As shown in Fig. 3, the CA curves depict the charge density of Li^+ ions as a function of time for these two films under pulsed potentials of 1.0 V and −1.3 V, each applied for 30 seconds. During the coloration process, the Li^+ ions intercalate into the working electrode films from the $LiClO_4$ electrolyte. When the process transitions from coloration to bleaching, the Li^+ ions are deintercalated back into the electrolyte. As illustrated in Fig. 3a and b, within a single bleaching/coloration cycle, the charge density rapidly decreases within a few seconds, decaying from approximately 2.45 to −3.18 mC cm^{-2} for the WO_3 film and from 1.92 to −3.81 mC cm^{-2} for the WO_3/PBI hybrid film. The corresponding change values are approximately 5.64 mC cm^{-2} (WO_3 film, denoted as Q1-1) and 5.74 mC cm^{-2} (WO_3/PBI hybrid film, denoted as Q2-1). After 500 cycles, the charge density of the WO_3 film varies from 0.75 to −1.91 mC cm^{-2}, with a corresponding change value of ~2.67 mC cm^{-2} (denoted as Q1-500). For the WO_3/PBI hybrid film, after 1400 cycles, the charge

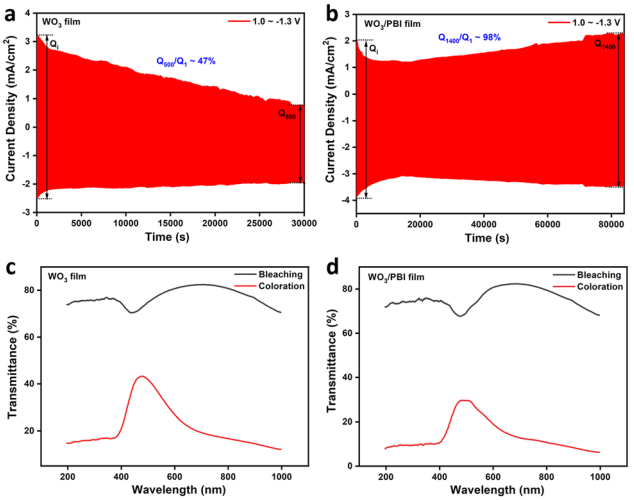

Fig. 3 Chronoamperometry curves of WO_3 (a) and WO_3/PBI hybrid films (b) in 1 mol L^{-1} $LiClO_4$/PC electrolyte. Optical transmittance difference (ΔT = $T_{colored}$ − $T_{bleached}$); corresponding UV-vis transmittance spectra of the WO_3 (c) and WO_3/PBI hybrid films (d) in colored and bleached states between 200 nm and 1000 nm.

density changes from 2.21 to −3.43 mC cm^{-2}, with a corresponding change value of ~5.64 mC cm^{-2} (denoted as Q2-1400). Reversibility is determined by the ratio Q_{di}/Q_i, yielding values of approximately 98% for the WO_3/PBI hybrid film (after 1400 cycles) and 47% for the WO_3 film (after 500 cycles).[26,28] Clearly, the WO_3/PBI hybrid film outperforms the pure WO_3 film in terms of both charge density (Q_i) and reversibility (Q_{di}/Q_i), indicating that the incorporation of PBI derivatives enhances the coloring/bleaching stability of the WO_3 film. It is demonstrated that the electrochromic performance of the degraded WO_3 film can be effectively rejuvenated through the incorporation of PBI derivatives.

To further evaluate the EC performance, the optical contrast (ΔT), response time and cycle stability of these two films were recorded during the CA process. The transmittance in Fig. 3c and d shows the colored and bleached states of the WO_3 and WO_3/PBI hybrid films over the wavelength range of 200–1000 nm, obtained under pulsed potentials of 1.0 V and −1.3 V, each applied for 30 seconds. The corresponding spectro-electrochemical transmittance spectra are displayed in Fig. 4. Both films exhibit relatively high transmittance (~80%, at 720 nm) across a broad wavelength range of 200–1000 nm in their bleached states. Additionally, the transmittance spectrum of the WO_3/PBI hybrid film clearly shows the characteristic peak of the PBI group, but no radical anion ($PBI^{\bullet-}$) or dianion (PBI^{2-}) appears in this electrochemical process.[29] As shown in Fig. S10, the WO_3/PBI hybrid film exhibits a larger transmittance modulation (~69.8% at 720 nm) compared to 63.8% for the pure WO_3 film.

The transmittance of the WO_3 film sharply decreases, dropping from 63.8% to 43.5% (maintaining ~68%) after 25 redox cycles, whereas the WO_3/PBI film maintains appropriate 91% transmittance after 1400 redox cycles (Fig. 5a and b).

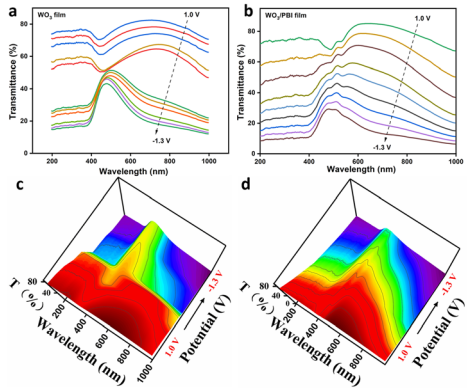

Fig. 4 Spectroelectrochemical spectra and spectral changes of the WO_3 (a and c) and WO_3/PBI hybrid films (b and d) at multi-step potentials between 1.0 and −1.3 V with a step time of 30 s.

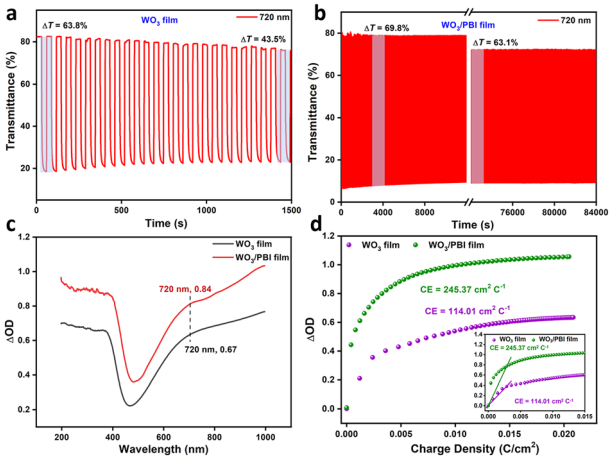

Fig. 5 Change in optical transmittance *vs.* time of the WO_3 (a) and WO_3/PBI (b) films obtained by applying pulsed potentials of 1.0 to −1.3 V for 30 s for each state at 720 nm; optical density (c) and CE (d) curves of the WO_3/PBI hybrid film at a wavelength of 720 nm.

Furthermore, a large optical density modulation (ΔOD), defined as the ratio of the transmittance at the bleached state to that at the colored state, of 0.84 was achieved for the WO_3/PBI hybrid film, compared to 0.67 for the WO_3 film, confirming its superior coloration ability (Fig. 5c).

The switching speed, defined as the time required to reach 90% of optical modulation during the coloring or bleaching process, is similar for both films: 5.0 s and 1.2 s for the WO_3/PBI hybrid film and 5.4 s and 0.9 s for the pure WO_3 film (Fig. S11).

The coloration efficiency is calculated using the formulae[30,31]

$$CE(\lambda) = \Delta OD/\Delta Q$$

$$\Delta OD = \log(T_b/T_c)$$

where ΔOD represents the change in optical density, ΔQ is the inserted charge, T_b is the transmittance at the bleached state,

and T_c is the transmittance at the colored state. ΔQ can be determined by integrating the current density over the coloration time. The coloration efficiency of the WO_3/PBI film (245 cm^2 per C) is more than double that of the WO_3 film (114 cm^2 per C) (Fig. 4d). The excellent cycling durability and coloration efficiency of the hybrid film are attributed to three factors: (1) surface modification by the organic component, (2) an enhanced diffusion coefficient and (3) improved electrochemical activity achieved through PBI-CB derivative incorporation.[32,33]

Experimental

Materials and instrumentation

All the chemicals were purchased from Sinopharm Chemical Reagent Co., Ltd, were analytical grade and used without further purification. The compounds were synthesized and characterized according to a previous report.[34] The morphologies of the PBI-CB films were characterized using a field emission scanning electron microscope (SEM, Hitachi SU8220, 5 kV). The structural properties of the films were analysed using X-Ray Diffraction (XRD, D8 Advance) measurements over a 2θ diffraction angle range of 10°–55°. ITO substrates (~9 Ω cm^{-2}, 0.9 cm × 4 cm) were washed successively with acetone, ethanol and deionized water and then thoroughly dried under a nitrogen flow.

Preparation of pure WO_3 films

The pure WO_3 film was prepared according to previously reported methods.[35,36] Briefly, 5 μL of H_2O_2 was mixed with 8 mL of a 0.125 mol L^{-1} Na_2WO_4 solution, followed by the addition of 1 mol L^{-1} H_2SO_4 to reach a final volume of 10 mL, forming the electrolyte. The electrochemical synthesis of the pure WO_3 film was conducted using a two-electrode system, with a CHI 660E serving as the power source. The film was deposited onto an ITO-coated glass substrate at a constant current density of 2 mA cm^{-2} for various durations, employing a Pt sheet as the counter electrode. After solvent evaporation, transparent to yellow films were obtained.

Preparation of hybrid WO_3/PBI films

A stock solution of PBI-CB (1.0×10^{-3} mol L^{-1}) was prepared by dissolving an appropriate amount of PBI-CB in chloroform. The stock solution was then drop-coated onto pristine WO_3 films and air-dried at ambient temperature. Subsequently, hybrid WO_3/PBI films were obtained by annealing the dried films at various temperatures for 2 h under vacuum conditions. This process yielded hybrid WO_3/PBI films with varying compositions.

Electrochemical measurement

The electrochemical behaviour of hybrid WO_3/PBI films deposited on ITO substrates was investigated using cyclic voltammetry (CV). Experiments were conducted in a three-electrode system, with the WO_3/PBI-coated ITO serving as the working electrode, a platinum wire as the counter electrode, and an Ag/AgCl electrode as the reference electrode. CV curves were recorded by scanning from 1.0 V to −1.3 V at a scan rate of 50 mV s^{-1}. Spectroelectrochemical measurements were performed using a CHI-660E electrochemical workstation (Shanghai Chenhua Instrument Co. Ltd) coupled with a fiber optic spectrometer (QEpro, Ocean Optics). All measurements were conducted under quiescent conditions in a supporting electrolyte of 1 mol L^{-1} LiClO4 dissolved in a propylene carbonate/acetonitrile mixture at room temperature.

Conclusions

In summary, an organic/inorganic EC material was constructed by dip-coating PBI derivatives onto the surface of WO_3 films *via* an orthogonal design strategy. Orthogonal design-based mathematical analysis identified the key factors influencing the experimental results and determined the optimal combination of factor levels. The integration of PBI derivatives significantly enhanced the performance of the WO_3 film: the hybrid surface became more continuous and compact, which improved ionic/electrical conductivity and accelerated the reaction kinetics of WO_3 in the electrolyte. The resultant WO_3/PBI hybrid film exhibited superior charge density and reversibility, indicating that the introduction of PBI derivatives effectively enhanced the coloration/bleaching stability of pure WO_3 films. Additionally, the WO_3/PBI hybrid film exhibited a high coloration efficiency, attributed to the geometrical confinement effect induced by the formation of inorganic/organic aggregates. Our results demonstrate a simple strategy to design and construct hybrid materials for high-performance EC systems.

Author contributions

Chunxia Hua: writing – original draft, visualization, conceptualization, data curation, formal analysis, investigation, and methodology. Huanyu Tan: investigation and resources. Shujin Ma: investigation and methodology. Jiaxu Hou: investigation and methodology. Jia Chu: writing – review & editing and formal analysis. Ming Gong: software and resources. Xiaoqin Wang: formal analysis. Shanxin Xiong: project administration, writing – review & editing, conceptualization, supervision, and funding acquisition.

Conflicts of interest

There are no conflicts to declare.

Data availability

The data that support the findings of this study are available from the corresponding author upon reasonable request: experimental details, detailed synthesis procedures, characterization

data of the compounds, and supplementary schemes, figures and tables. See DOI: https://doi.org/10.1039/d5dt01423a.

Acknowledgements

The authors thank the National Natural Science Foundation of China (22102093, 52073227 and 22303065) and the Qin Chuangyuan High-Level Innovative and Entrepreneurial Talents Recruitment Program (QCYRCXM-2023-054) for their financial support.

References

1 Y. Zhai, J. Li, S. Shen, Z. Zhu, S. Mao, X. Xiao, C. Zhu, J. Tang, X. Liu and J. Chen, Recent Advances on Dual–Band Electrochromic Materials and Devices, *Adv. Funct. Mater.*, 2022, **32**(17), 2109848.

2 H. Anyang, J. Zhisen, K. Chunguang, S. Mcguigan, D. Nordlund, L. Yijin and F. Lin, Uncovering Phase Transformation, Morphological Evolution, and Nanoscale Color Heterogeneity in Tungsten Oxide Electrochromic Materials, *J. Mater. Chem. A*, 2020, **8**, 20000.

3 F. Xueying, A. Kuchmizhak, L. Pattelli, L. Yao and X. Hongbo, Resolving Molecular Size and Homologues with a Self-Assembled Metal-Organic Framework Photonic Crystal Detector, *ACS Mater. Lett.*, 2023, **5**, 1703.

4 Z. Shao, A. Huang, C. Ming, J. Bell, P. Yu, Y. Sun, L. Jin, L. Ma, H. Luo, P. Jin and X. Cao, All-Solid-State Proton-Based Tandem Structures for Fast-Switching Electrochromic Devices, *Nat. Electron.*, 2022, **5**(1), 45.

5 F. Xueying, P. Huan and X. Hongbo, Ni-IRMOF-74 film for Fast-Switching and High-Stability Electrochromic, *ACS Energy Lett.*, 2024, **9**, 2840.

6 C. Hua, S. Dou, H. Xu, S. Hou, H. Zhang, P. Zhang, Y. Gan, J. Zhao and Y. Li, A Nanostructured $Fc(COCH_3)_2$ Film Prepared Using Silica Monolayer Colloidal Crystal Templates and Its Electrochromic Properties, *Phys. Chem. Chem. Phys.*, 2017, **19**(45), 30756.

7 D. Dalavi, R. Desai and P. Patil, Nanostructured Materials for Electrochromic Energy Storage Systems, *J. Mater. Chem. A*, 2022, **10**, 1179.

8 A. Shchegolkov, S. Jang, A. Shchegolkov, Y. Rodionov, A. Sukhova and M. Lipkin, A Brief Overview of Electrochromic Materials and Related Devices: A Nanostructured Materials Perspective, *Nanomaterials*, 2021, **11**(9), 2376.

9 M. Jo, K. Kim and H. Ahn, P-Doped, Carbon Quantum Dot Graft-Functionalized Amorphous WO_3 for Stable and Flexible Electrochromic Energy-Storage Devices, *Chem. Eng. J.*, 2022, **445**, 136826.

10 R. Wen, C. Granqvist and G. Niklasson, Eliminating Degradation and Uncovering Ion-Trapping Dynamics in Electrochromic WO_3 Thin Films, *Nat. Mater.*, 2015, **14**(10), 996.

11 T. Hao, S. Wang, H. Xu, X. Zhang, J. Xue, S. Liu, Y. Song, Y. Li and J. Zhao, Stretchable Electrochromic Devices Based on Embedded WO_3@AgNW Core-Shell Nanowire Elastic Conductors, *Chem. Eng. J.*, 2021, **426**, 130840.

12 X. An, J. Yu, Y. Wang, Y. Hu, X. Yu and G. Zhang, WO_3 Nanorods/Graphene Nanocomposites for High-Efficiency Visible-Light-Driven Photocatalysis and NO_2 Gas Sensing, *J. Mater. Chem.*, 2012, **22**(17), 8525.

13 S. Wang, H. Xu, J. Zhao and Y. Li, Two-Dimensional WO_3 Nanosheets for High-Performance Electrochromic Supercapacitors, *Inorg. Chem. Front.*, 2022, **9**(3), 514.

14 Z. Wang, X. Wang, S. Cong, J. Chen, H. Sun, Z. Chen, G. Song, F. Geng, Q. Chen and Z. Zhao, Towards Full-Colour Tunability of Inorganic Electrochromic Devices using Ultracompact Fabry-Perot Nanocavities, *Nat. Commun.*, 2020, **11**(1), 302.

15 V. Thakur, G. Ding, J. Ma, P. Lee and X. Lu, Hybrid Materials and Polymer Electrolytes for Electrochromic Device Applications, *Adv. Mater.*, 2012, **24**(30), 4071.

16 G. Phan, D. Pham, R. Patil, C. Tsai, C. Lai, W. Yeh, Y. Liou and Y. Ma, Fast-Switching Electrochromic Smart Windows Based on NiO-Nanorods Counter Electrode, *Sol. Energy Mater. Sol. Cells*, 2021, **231**, 111306.

17 Y. Yang, Y. Qi, W. Zhai, J. Tan, S. Feng, J. Zhang, M. Shen, X. Wang, L. Yu and X. Qu, Enhanced Electrochromic Performance of Film Based on PreysslerType Polyoxometalate and Tungsten Oxide, *Electron. Mater. Lett.*, 2020, **16**, 424.

18 G. Cai, J. Tu, D. Zhou, J. Zhang, X. Wang and C. Gu, Dual Electrochromic Film based on WO_3/Polyaniline Core/Shell Nanowire Array, *Sol. Energy Mater. Sol. Cells*, 2014, **122**, 51.

19 C. Hua, K. Liu, Y. Wu, W. Xu, J. Zhang, Z. Wang, K. Liu and Y. Fang, An O-Carborane Derivative of Perylene Bisimide-Based Thin Film Displaying Both Electrochromic and Electrofluorochromic Properties, *ACS Appl. Mater. Interfaces*, 2021, **13**(41), 49500–49508.

20 L. Zhang, Z. Mu and X. Gao, Coupling Analysis and Performance Study of Commercial 18650 Lithium-Ion Batteries under Conditions of Temperature and Vibration, *Energies*, 2018, **11, 10**, 2856.

21 J. Zhang, J. Tu, D. Zhang, Y. Qiao, X. Xia, X. Wang and C. Gu, Multicolor Electrochromic Polyaniline-WO_3 Hybrid Thin Films: One-Pot Molecular Assembling Aynthesis, *J. Mater. Chem.*, 2011, **21, 43**, 17316.

22 X. Liu, J. Wang, D. Tang, Z. Tong, H. Ji and H. Qu, A Forest Geotexture-Inspired ZnO@Ni/Co Layered Double Hydroxide-Based Device with Superior Electrochromic and Energy Storage Performance, *J. Mater. Chem. A*, 2022, **10**(23), 12643.

23 D. Mawhinney and J. Yates, FTIR Study of the Oxidation of morphous Carbon by Ozone at 300 K-Direct COOH Formation, *Carbon*, 2001, **39**, 1167.

24 X. Deng, Z. Fang, Y. Liu and C. Yu, Production of Biodiesel from Jatropha Oil Catalyzed by Nanosized Solid Basic Catalyst, *Energies*, 2011, **36**(2), 777.

25 J. Gonzalez and J. Sequí-Castellano, Electrochemical Determination of Kinetic Parameters of Surface Confined Redox Probes in Presence of Intermolecular Interactions by Means of Cyclic Voltammetry. Application to TEMPO

Monolayers in Gold and Platinum Electrodes, *Electrochim. Acta*, 2021, **365**, 137331.
26 R. Patil, R. Devan, Y. Liou and Y. Ma, Efficient Electrochromic Smart Windows of One-Dimensional Pure Brookite TiO_2 Nanoneedles, *Sol. Energy Mater. Sol. Cells*, 2016, **147**, 240.
27 Z. Deng, H. Jiang, Y. Hu, Y. Liu, L. Zhang, H. Liu and C. Li, 3D Ordered Macroporous MoS_2@C Nanostructure for Flexible Li-Ion Batteries, *Adv. Mater.*, 2017, **29**, 1603020.
28 R. Patil, R. Devan, J. Lin, Y. Ma, P. Patil and Y. Liou, Efficient Electrochromic Properties of High-Density and Large-Area Arrays of One-Dimensional NiO Nanorods, *Sol. Energy Mater. Sol. Cells*, 2013, **112**, 91.
29 X. Lv, L. Zha, L. Qian, X. Xu, Q. Bi, Z. Xu, D. Wright and C. Zhang, Controllable Fabrication of Perylene Bisimide Self-Assembled Film and Patterned All-Solid-State Electrochromic Device, *Chem. Eng. J.*, 2020, **386**, 123939.
30 S. Heo, C. Dahlman, C. Staller, T. Jiang, A. Dolocan, B. Korgel and D. Milliron, Enhanced Coloration Efficiency of Electrochromic Tungsten Oxide Nanorods by Site Selective Occupation of Sodium Ions, *Nano Lett.*, 2020, **20**(3), 2072.
31 D. Bessinger, K. Muggli, M. Beetz, F. Auras and T. Bein, Fast-Switching Vis-IR Electrochromic Covalent Organic Frameworks, *J. Am. Chem. Soc.*, 2021, **143**(19), 7351.
32 C. Gu, S. Wang, J. He, Y. Zhang and X. Zhang, High-Durability Organic Electrochromic Devices Based on *In situ*-hotocurable Electrochromic Materials, *Chem*, 2023, **9**, 2841.
33 S. Kao, H. Lu, C. Kung, H. Chen, T. Chang and K. Ho, Thermally Cured Dual Functional Viologen-Based All-In One Electrochromic Devices with Panchromatic Modulation, *ACS Appl. Mater. Interfaces*, 2016, **8**, 4175.
34 K. Liu, C. Shang, Z. Wang, Y. Qi, R. Miao, K. Liu, T. Liu and Y. Fang, Non-Contact Identification and Differentiation of Illicit Drugs using Fluorescent Films, *Nat. Commun.*, 2018, **9**(1), 1695.
35 B. Yang, P. Barnes, W. Bertram and V. Luca, Strong hotoresponse of Nanostructured Tungsten Trioxide Films Prepared via a Sol-Gel Route, *J. Mater. Chem.*, 2007, **17**, **26**, 2722.
36 S. Hassab and J. Padilla, Using WO_3 as a Transparent, Optically-Passive Counter Electrode in An Unbalanced Electrochromic Configuration, *Electrochem. Commun.*, 2016, **72**, 87.